

OPEN ACCESS

Electrode Blocking Due to Redox Reactions in Aluminum Chloride-Sodium Iodide Molten Salts

To cite this article: Adam M. Maraschky *et al* 2023 *J. Electrochem. Soc.* **170** 066504

View the [article online](#) for updates and enhancements.

You may also like

- [Continuous Purification of Molten Chloride Salt: Electrochemical Behavior of MgOHCl Reduction](#)
Liam Witteman, Kerry Rippy, Patrick Taylor et al.
- [Study on Stable Lithiophilic Ag Modification Layer on Copper Current Collector for High Coulombic-Efficiency Lithium Metal Anode](#)
He-yi Xia, Dong-lei Wang, Yu-ke Wang et al.
- [Enhancing Electrochemical Performance of Zinc-Air Batteries Using Freeze Crosslinked Carboxymethylcellulose-Chitosan Hydrogels as Electrolytes](#)
María Fernanda Bósquez-Cáceres, José Bejar, Lorena Álvarez-Contreras et al.

Your Lab in a Box!

The PAT-Tester-i-16: All you need for Battery Material Testing.

- ✓ **All-in-One Solution with Integrated Temperature Chamber (10-80°C)!**
No additional devices are required to measure at a stable ambient temperature.
- ✓ **Fully featured Multichannel Potentiostat / Galvanostat / EIS!**
Up to sixteen independent battery test channels, no multiplexing.
- ✓ **Ideally suited for High-Precision Coulometry!**
Measure with excellent accuracy and signal-to-noise ratio at the same time.
- ✓ **Small Footprint, Easy to Setup and Operate!**
Cableless connection of 3-electrode battery test cells. Full multi-user, multi-device control via LAN.



EL-CELL®
electrochemical test equipment

Learn more on our product website:



Download the Data Sheet (PDF):



Or contact us directly:

☎ +49 40 79012-734

✉ sales@el-cell.com

🌐 www.el-cell.com



Electrode Blocking Due to Redox Reactions in Aluminum Chloride-Sodium Iodide Molten Salts

Adam M. Maraschky,^{1,*} Stephen J. Percival,^{1,*} Rose Y. Lee,^{1,2,*} Melissa L. Meyerson,^{1,*} Amanda S. Peretti,¹ Erik D. Spörcke,^{1,*} and Leo J. Small^{1,z,*}

¹Sandia National Laboratories, Albuquerque, New Mexico 87185, United States of America

²Department of Chemical Engineering, University of Washington, Seattle, Washington 98195, United States of America

Iodide redox reactions in molten NaI/AlCl₃ are shown to generate surface-blocking films, which may limit the useful cycling rates and energy densities of molten sodium batteries below 150 °C. An experimental investigation of electrode interfacial stability at 110 °C reveals the source of the reaction rate limitations. Electrochemical experiments in a 3-electrode configuration confirm an increase of resistance on the electrode surface after oxidation or reduction current is passed. Using chronopotentiometry, chronoamperometry, cyclic voltammetry, and electrochemical impedance spectroscopy, the film formation is shown to depend on the electrode material (W, Mo, Ta, or glassy carbon), as well as the Lewis acidity and molar ratio of I[−]/I₃[−] in the molten salt electrolytes. These factors impact the amount of charge that can be passed at a given current density prior to developing excessive overpotential due to film formation that blocks the electrode surface. The results presented here guide the design and use of iodide-based molten salt electrolytes and electrode materials for grid scale battery applications.

© 2023 The Author(s). Published on behalf of The Electrochemical Society by IOP Publishing Limited. This is an open access article distributed under the terms of the Creative Commons Attribution 4.0 License (CC BY, <http://creativecommons.org/licenses/by/4.0/>), which permits unrestricted reuse of the work in any medium, provided the original work is properly cited. [DOI: 10.1149/1945-7111/acd874]



Manuscript submitted February 1, 2023; revised manuscript received April 24, 2023. Published June 5, 2023. *This paper is part of the JES Focus Issue on Molten Salts and Ionic Liquids III.*

Supplementary material for this article is available [online](#)

Molten sodium batteries (MNaBs) with metal halide-sodium iodide electrolytes have emerged as an Earth-abundant,¹ cost-effective, and safe technology for grid scale electrochemical energy storage.^{2,3} This class of low-temperature (<150 °C) MNaBs is enabled by a Na-ion superconductor (NaSICON, nominally Na_{1+x}Zr₂Si_xP_{3-x}O₁₂) solid electrolyte,^{4–6} which physically separates the Na metal anode from the molten salt electrolyte.^{7,8} Mixtures of NaI and AlCl₃ offer relatively inexpensive, nonflammable, highly conductive (>100 mS cm^{−1}), highly concentrated (>4 mol l^{−1}), redox-active electrolytes at temperatures slightly above the melting point of Na metal (98 °C). Despite these advantages, achieving the high cycling rates needed for on-demand, high-rate energy storage applications may present challenges for this molten salt chemistry at low temperatures (<150 °C).

Pairing the iodide redox couple with alkali metal anodes in nonaqueous electrolytes for a battery cell >3 V was investigated by Hanson and Tobias in 1987.⁹ More recently, iodide electrochemistry has seen applications in Zn/I₂ redox flow batteries,^{10–13} room temperature ionic liquid electrolytes,¹⁴ and dye-sensitized solar cells.^{15,16} Much of the research on iodide electrochemistry has been devoted to discerning the reaction mechanisms,^{17–19} characterizing the electrocatalytic activity of electrode materials,^{16,20,21} and understanding polyiodide film formation during iodide oxidation.^{9–11,22–26} This prior work provides guidance for applications of I[−]/I₃[−]/I₂ redox reactions, which are known to be highly dependent on the solvent^{22,27,28} and concentration.²⁰ For low-temperature MNaBs with NaI/AlCl₃ electrolytes in particular, the species and phases present depend on the electrolyte composition, which varies with the battery's state of charge (SoC) via the ratio of I[−] to higher order polyiodides such as I₃[−].^{28,29} Understanding the complex and interrelated physicochemical behavior of these systems requires careful analysis of what processes limit the cycling rate at temperatures and electrolyte compositions relevant to practical battery operation.

The present investigation seeks to clarify the roles that (i) electrode material and (ii) molten salt composition play in the electrochemistry of iodide in NaI/AlCl₃ electrolytes. Achieving this understanding will

provide a better mechanistic picture of whether the redox reaction rates are limited by mass transport, charge transfer kinetics, or electrode surface changes, such as adsorption or blocking. This understanding will aid in identifying what engineering solutions can be used to improve the battery's energy efficiency and power density. Toward this goal, we investigate the NaI/AlCl₃ system using cyclic voltammetry (CV), electrochemical impedance spectroscopy (EIS), chronoamperometry (CA), and chronopotentiometry (CP). The 3-electrode configuration employed here isolates the electrode in contact with the molten salt electrolyte.²⁹ Although the selection of materials chemically compatible with the NaI/AlCl₃ electrolyte is limited, we examine three refractory metals: tungsten (W), molybdenum (Mo), and tantalum (Ta), as well as glassy carbon (GC) as candidate electrode materials. Ideally, these materials need to be not only chemically inert in the electrolyte, but cost-effective and electrocatalytically active. The electrochemical behavior of the candidate electrodes is examined at two SoCs (7.5 and 50%) and two molar ratios of the NaI/AlCl₃ electrolyte (nominally, Lewis acidic and Lewis basic). Results show that electrode materials and electrolyte compositions differ most notably in their susceptibility to blockage caused by reversible surface film formation during electrolysis. Electrolyte composition—through both Lewis acidity and SoC—impacts the phase stability of electrochemical reaction products and their tendency to form electrode-blocking films. These insights will guide the future development of low-temperature MNaBs for sustainable grid scale energy storage.

Experimental

Electrolyte composition.—Electrolytes were made by mixing NaI (ultra-dry, 99.99%, Alfa Aesar), AlCl₃ (ultra-dry, 99.99%, Alfa Aesar), and I₂ (ultra-dry, 99.998%, Alfa Aesar), all of which were used without further purification and were handled in an Ar-filled glovebox with <0.1 ppm H₂O and O₂. Electrolyte compositions are listed in Table I. The theoretical capacity of the electrolyte is determined by $C = zFn$, where F is the Faraday constant, n is the number of moles of NaI for a fully discharged (0% SoC) electrolyte, and z is the number of electrons per mole of I₃[−] in the reaction:



Equation 1 is an idealized reaction for this system and may not represent the actual species present in the electrolyte since I[−] is

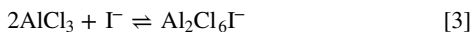
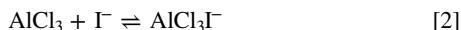
*Electrochemical Society Member.

^zE-mail: ammaras@sandia.gov; ljsmall@sandia.gov

Table I. Electrolyte compositions used in 3-electrode cells.

State of charge (% SoC)	Nominal composition	Theoretical capacity (Ah)	Mass NaI (g)	Mass AlCl ₃ (g)	Mass I ₂ (g)	mol% NaI	mol% AlCl ₃	mol% I ₂
7.5	Acidic	3.000	23.91	27.36	1.07	43.2	55.6	1.14
50	Acidic	3.000	16.78	27.36	7.10	32.4	59.5	8.11
7.5	Basic	4.000	31.88	19.90	1.42	57.9	40.6	1.52
50	Basic	4.000	22.37	19.90	9.47	44.4	44.4	11.1

known to complex with AlCl_3 , forming Lewis adducts,^{28–31}



The nominal composition of the electrolyte denotes the Lewis acidity, where Lewis acidic compositions are >50 mol% AlCl_3 , while Lewis basic compositions are <50 mol% AlCl_3 . The Lewis acidity determines the species present in the electrolyte. For instance, dimeric species (e.g., $\text{Al}_2\text{Cl}_6\text{I}^-$ formed via Eq. 3) are present in significant quantities only in acidic mixtures.^{29,31} The electrolytes were mixed in a partially charged state by substituting the desired charged fraction f of half the moles of NaI n with I_2 . The added I_2 is assumed to react in the presence of excess I^- to form I_3^- via the reaction³²



Again, Eq. 4 may not reflect the actual species present in the molten salt due to complexation²⁸ with AlCl_3 . However, Eqs. 1 and 4 are useful for tracking the theoretical SoC. The amount of NaI added to the cell n' was adjusted from n to account for the charged fraction f added as I_2 : $n' = n(1 - fz)$. The large capacity of the electrolytes prevented significant changes in SoC during experiments. The Lewis basic electrolytes had higher theoretical capacity than the acidic ones due to the higher mol% NaI in equivalent total electrolyte volumes. The SoC chosen for these experiments (7.5 and 50%) represent low and high values of the cycled capacity for this class of MNABs.^{3,29}

Separator and sodium metal preparation.—NaSICON separators were fabricated as described previously.²⁹ After polishing to 1200 grit, one side of the NaSICON was sputtered with 200 nm of Sn, as described and demonstrated elsewhere.⁸ The area of the coating (1.13 or 1.77 cm^2) was defined by shadow masks. The Na metal used in electrodes was purified by removing the native oxide with a razor blade, followed by melting the Na, syphoning the pure metal, and leaving behind the oxidized residue. The purified Na metal was saturated with Sn (6.7×10^{-3} wt%) to prevent dissolution of the Sn film deposited on the NaSICON.⁷

Working electrode preparation.—Rod materials were purchased from Alfa Aesar with the following diameters and purity: W (0.125 in, 99.95%, annealed), Mo (0.125 in, 99.95%, annealed), Ta (0.11 in, 99.95%), and GC (0.16 in, type 2). Disk electrodes were prepared by (1) wet polishing one end of the rod to 1200 grit with SiC paper, (2) sealing the end of the rod with PTFE heat shrink tubing, (3) removing the excess tubing to expose a disk, followed by (4) polishing sequentially with 1.0, 0.3, and 0.05 μm alumina slurries. Sonication in deionized water was used between polishing steps before final sonication and rinsing in isopropanol.

Cell construction.—The custom 3-electrode cell used in all experiments is depicted in Fig. 1. This cell contained the molten salt electrolyte in a central glass column with 3 glass o-ring joints (Adams & Chittenden), as described previously.²⁹ The two facing joints were clamped to chambers containing Na metal, each separated by one 0.9 mm thick NaSICON pellet. The large Na chamber was used as the counter electrode (CE) while the small Na chamber was used as the reference electrode (RE). The Sn coating on the NaSICON facing the Na of the CE had a geometric area of 1.77 cm^2 , while that on the RE had an area of 1.13 cm^2 . Tungsten (W) rods glass-sealed to the ends of these chambers were used as electrical contacts for the Na metal. The top joint of the central column was covered by a machined PTFE top with a compression fitting that allowed the height of the working electrode (WE) rod to be adjusted into or out of the molten salt. Polymeric O-rings were used to compression seal the glass joints and the NaSICON or PTFE top. EPDM O-rings were used on sides containing Na metal, while

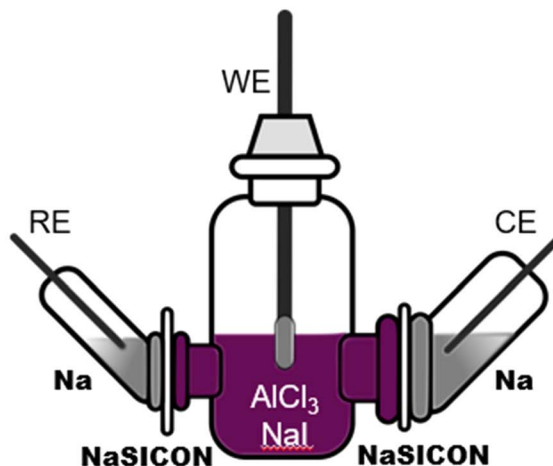


Figure 1. Schematic and photograph of the 3-electrode cell. Scale bar (white) is 3.5 cm. Metallic Na-containing chambers (grey) were separated from the molten salt-containing central column (purple) by NaSICON disks (white). The 3-electrode cell was operated in an oven at 110 °C inside an Ar-filled glovebox.

PTFE were used on sides containing salt. The NaI and AlCl_3 powders were thoroughly blended with a spatula before melting in the central chamber of the cell overnight. The molten salt was allowed to cool to room temperature before adding I_2 . The cell's hermetic seal, which confined the volatile I_2 gas, enabled 3-electrode examination of iodide electrochemistry in NaI/AlCl_3 electrolytes above 0% SoC. Cells were assembled and used in an Ar-filled glovebox with <0.1 ppm O_2 and H_2O .

Electrochemical measurements.—Electrochemical measurements were performed using a Solartron ModuLab XM ECS potentiostat connected to the 3-electrode cells, which were operated inside a convection oven at 110 °C inside the glovebox. Potentiostatic impedance measurements used 10 mV rms AC amplitude. Values for R_Ω and R_s were interpreted from the intersection of the Nyquist plot with the real axis. All voltages are reported V vs Na/Na^+ , except in cases where the E_{eq} was subtracted. Between CV runs, a ≥ 600 s rest period was used to allow the electrode to be refreshed.

Results and Discussion

In this section, the four electrode materials (W, Ta, Mo, and GC) are first screened in acidic NaI/AlCl_3 to assess their electrochemical performance and any electrocatalytic properties for I^-/I_3^- redox reactions. Electrochemical characterization in a 3-electrode cell is employed to understand what factors limit oxidation and reduction reactions in the electrolyte. Lewis acidic and basic electrolytes are

then compared at two states of charge to understand if and how the molten salt composition affects the electrode-electrolyte interfacial stability during redox reactions. Lastly, the mechanisms underlying the electrode instabilities and the times for refreshing the electrode surface are investigated.

Influence of electrode material in acidic electrolyte.—Figure 2 shows CVs collected in 3-electrode cells at 110 °C using W, Mo, GC, and Ta macroscale disk working electrodes between $V_{\text{app}} = 2.3$ and 3.6 V vs Na/Na⁺. Voltammetry was used here primarily to compare the redox behavior of the different materials qualitatively. Precise determination of kinetic parameters from these CVs would require numerical simulations.^{28,33–35} Ohmic losses were subtracted from the applied voltage using the ohmic resistance (R_{Ω}) measured by EIS, providing the potential at the electrode, $E_s = V_{\text{app}} - iR_{\Omega}$. Additional details about iR_{Ω} compensation, including uncorrected CVs (Fig. S1), are provided in the SI.

In acidic NaI/AlCl₃ electrolyte at 7.5% SoC, the four electrode materials all showed a single oxidative branch at the anodic potentials applied (Fig. 2). The oxidation reaction had an onset potential of $E_s = 3.17$ V, which was roughly independent of scan rate and electrode material. In contrast to relatively stable performance during iodide oxidation observed on the other materials, Mo had significant hysteresis between forward and reverse scans and deactivation behavior above $E_s = 3.3$ V at 10 mV s⁻¹. In this case, i decayed to 3 mA cm⁻² on the reverse scan (decreasing V_{app}). GC and W had the steepest slopes of the anodic i vs E_s branch. GC also had the most stable and consistent i vs E_s response at anodic potentials,

with minimal hysteresis between forward and reverse scans and negligible scan rate dependence. GC showed one strong cathodic peak potential E_{pc} between 3.08 V at 10 mV s⁻¹ and 3.11 V at 100 mV s⁻¹. The 3 refractory metals each had two prominent cathodic peaks on scans below 250 mV s⁻¹. For Mo, the E_{pc} at $E_s = 2.87$ V was roughly independent of scan rate. Mo had two additional cathodic peaks, which were most obvious at 50 mV s⁻¹, occurring at $E_s = 2.67$ and 2.51 V.

From the CV data in acidic electrolyte, GC clearly showed scan rate independence at anodic potentials, implying fast kinetics on I⁻ oxidation. Mo showed the most nuanced electrochemical behavior: unstable oxidative reactions, yet reversible kinetics and additional peaks at cathodic potentials $E_s < 3$ V. No material tested here showed significantly lower peak separation for the I⁻/I₃⁻ couple, as had been observed by Bentley et al. for Pt in a different iodide-based system.²⁰ Similarity between the reaction kinetics on W, Mo, and GC is supported by values of the charge transfer or surface resistance R_s (and therefore i_0)^{16,36} within 15% as determined from the Nyquist plots (Fig. S2).

Chronopotentiometry (CP) was used to evaluate the ability of the four electrode materials to maintain moderate current densities with consistently low overpotential, which is the desired behavior for efficient battery cycling. On reduction at -5 mA cm⁻², Mo showed the most stable voltage response of the four candidate electrode materials, with the least change in voltage from 0 to 900 s or 4.5 C cm⁻² (Fig. 3a). Ta and GC showed intermediate stability, while the voltage for W dropped to the cutoff, 2.3 V, after only 0.5 C cm⁻². It is noteworthy that the initial voltage during CP at -5 mA cm⁻² was roughly the same for all four materials. This

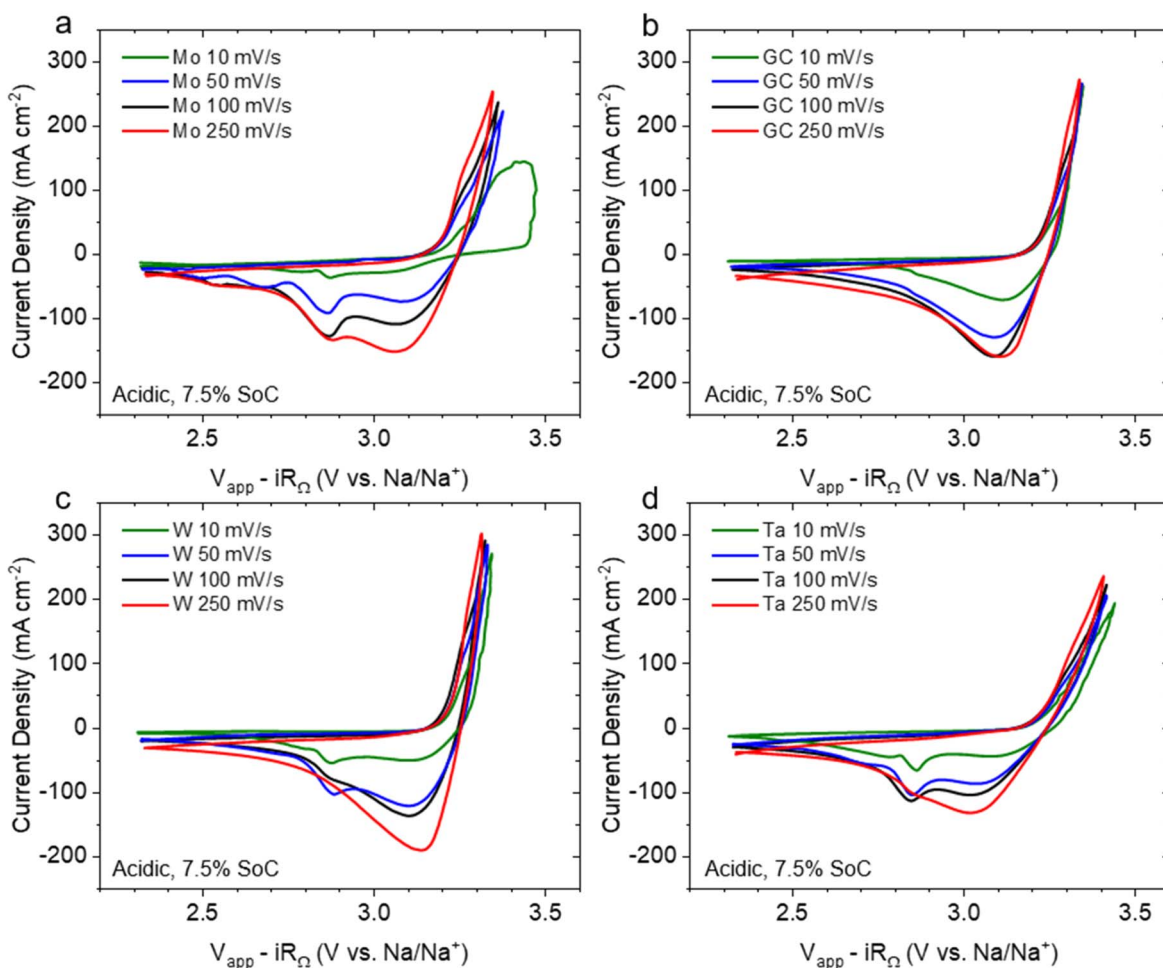


Figure 2. CVs obtained from acidic NaI/AlCl₃ with working electrode materials: (a) Mo, (b) GC, (c) W, (d) Ta. The iR_{Ω} drop was subtracted from the applied voltage V_{app} , which was swept between 2.3 to 3.6 V. The electrolyte was at 7.5% SoC. Scans were repeatable over multiple cycles; the second cycle is shown for each CV.

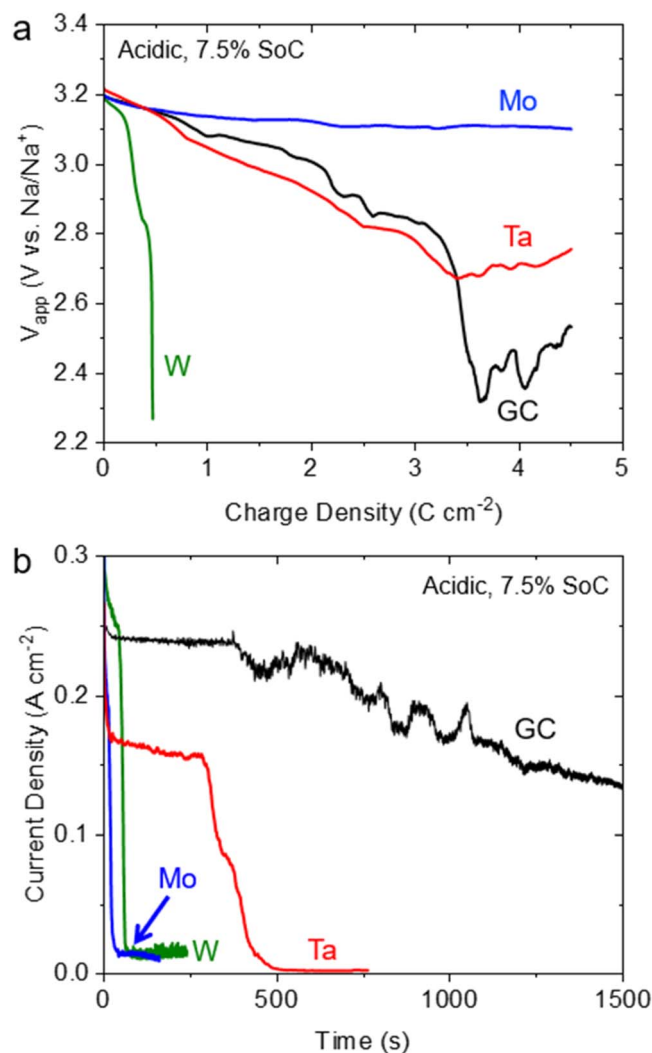


Figure 3. (a) CP at -5 mA cm^{-2} for up to 900 s on disk electrodes, W (green), GC (black), Ta (red), Mo (blue). The electrolyte was acidic NaI/AlCl₃ at 7.5% SoC and the cutoff V_{app} was 2.3 V vs Na/Na⁺. (b) CA at 3.6 V vs Na/Na⁺ obtained from the same electrolyte and electrodes in (a).

indicates that charge transfer kinetics and double layer charging, with characteristic times $<1 \text{ s}$, were similar while the electrodes were fresh, but that substantial changes occurred at the interface, affecting the voltage response during prolonged CP.

To compare each electrode material's efficiency for oxidation and reduction reactions, the final surface overpotential $\eta_s = E_s - E_{eq} = V_{app} - iR_\Omega - E_{eq}$ (after the 900 s of CP) was plotted as a function of i from ± 1 to 10 mA cm^{-2} on a polarization curve (Fig. S4). GC had the lowest η_s at $+10 \text{ mA cm}^{-2}$. However, the difference between materials on oxidation was minor compared to the disparity in reduction overpotentials at $i \leq -5 \text{ mA cm}^{-2}$ (Fig. 3a). Substantial increases in η_s occurred during reduction CP. In acidic electrolyte (NaI/AlCl₃ at 7.5% SoC), reduction was clearly more limited than oxidation due to instability at the electrode interface. This means that discharging a battery in this electrolyte composition could reach the voltage cutoff, or suffer from low energy efficiency, not because of changes in the bulk electrolyte (whose composition was not affected by the small charge passed during these experiments), but due to changes at the electrode-electrolyte interface. Mo was least susceptible to these interfacial changes during iodide reduction at -5 mA cm^{-2} . Mo also achieved the highest current density of the four candidate materials at a constant cathodic $V_{app} = 2.7 \text{ V}$ (Fig. S5).

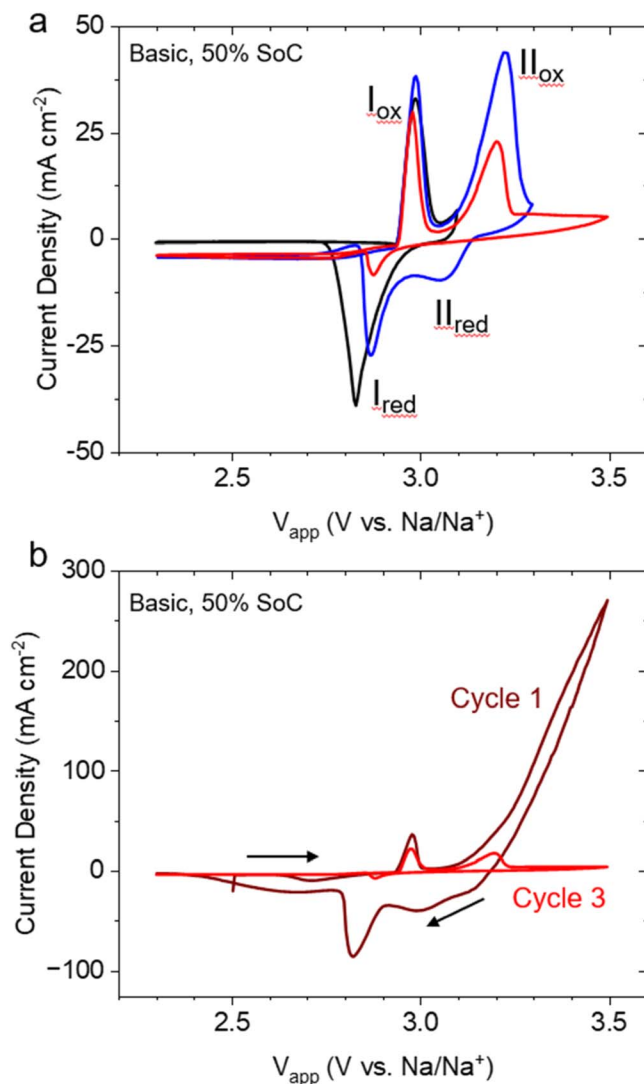


Figure 4. CVs obtained from basic NaI/AlCl₃ on a Mo disk at 10 mV s^{-1} . The electrolyte was at 50% SoC. (a) The anodic switching potential was increased from 3.10 V (black) to 3.30 V (blue) and 3.50 V (red). The CVs were repeated for multiple cycles until the behavior was stable. (b) Repeated cycles, 1 (dark red) and 3 (red), of the same conditions shown in (a), where the switching potential was also 3.50 V.

The relatively similar material performance of iodide oxidation identified using CV and EIS is contrasted in the results found by applying constant positive potential (CA) on disk electrodes (Fig. 3b). Here, 3.6 V was applied while the current was monitored. Of the four candidate materials, GC maintained the highest and slowest-decaying current density. Ta showed intermediate performance at first, but its steady state current after charge saturation and subsequent deactivation was much lower than the current at steady state for Mo and W. Notably, the initial i were all $>180 \text{ mA cm}^{-2}$ at time scales $t < 10 \text{ s}$, yet dropped to $<20 \text{ mA cm}^{-2}$ at longer times for Ta, Mo, and W but not GC.

In summary, the four candidate electrode materials sustained different amounts of charge before “shutting off” or becoming less active during redox reactions. Results suggest that changes occurred on the electrode surfaces, and that materials may have different abilities to resist interfacial changes. GC, Mo, and W had slight differences in charge transfer kinetics and CV behavior but differed widely in their electrochemical performance during CP at time scales relevant to battery operation. W had poor stability on both iodide oxidation and reduction, while Ta showed intermediate performance for both processes. However, the usefulness of Ta as a battery electrode is limited since the metal surface spontaneously formed an

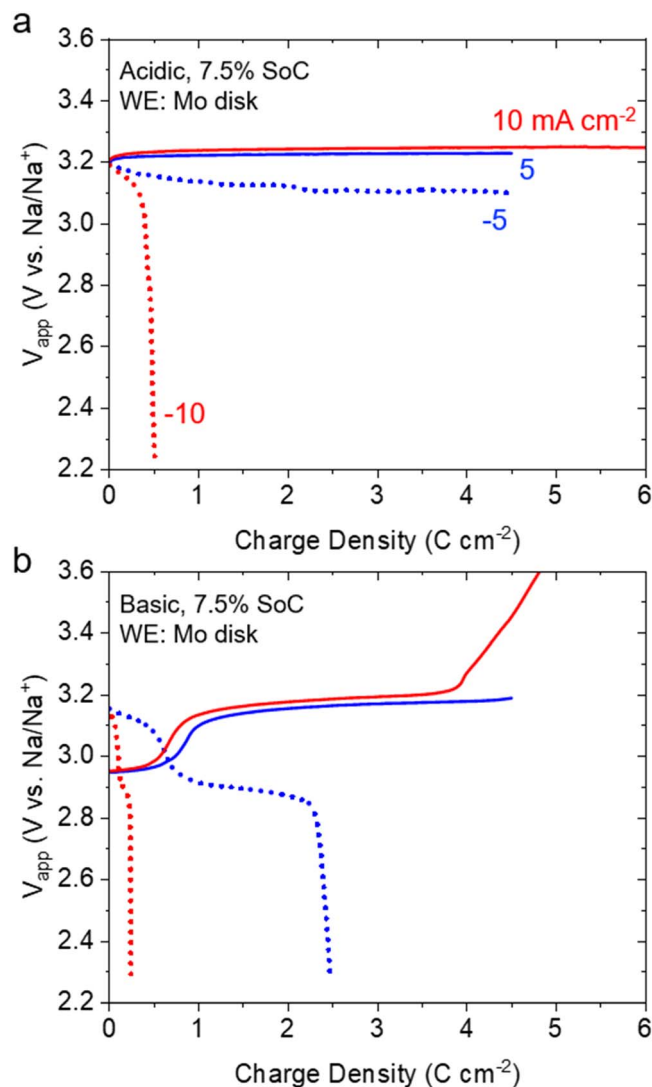


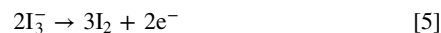
Figure 5. CP at 5 (blue) and 10 (red) mA cm^{-2} for up to 900 s on a Mo disk working electrode. The electrolytes were (a) acidic and (b) basic NaI/AlCl_3 , both at 7.5% SoC. Solid lines are positive (oxidation) current, while dotted lines are negative (reduction) current. Applied voltage limits were 2.3–3.6 V.

electrically insulating layer while in the glovebox, making it behave in a passivated manner compared to just after polishing (not shown for brevity). For these reasons, we down-selected further studies to the two most promising materials: GC for its more stable I^- oxidation and Mo for its more stable I_3^- reduction.

Voltammetric window-opening in basic NaI/AlCl_3 .—The preceding characterization was performed in Lewis acidic NaI/AlCl_3 , which is favorable from a physical standpoint since acidic compositions are fully molten at 110 °C whereas basic compositions have NaI solids (see the phase diagram in Fig. S6). However, Lewis acidic compositions of NaI/AlCl_3 have recently been shown to have a significant detrimental impact on charge transfer at the NaSICON/molten salt interface over time due to the presence of a dimeric $\text{Al}_2\text{Cl}_6\text{I}^-$ species.²⁹ While this prior study shows that Lewis basic NaI/AlCl_3 does not contain measurable dimeric species, thereby enabling effective NaSICON performance and battery cycling, it will be shown in the following sections using CV and CP that iodide redox reactions are more prone to cause electrode-electrolyte interfacial changes in basic electrolytes at 110 °C. This greater susceptibility to interfacial changes on oxidation is attributed in part to an additional redox couple not observed in acidic NaI/AlCl_3 .

Voltammetry scans to progressively higher anodic potentials shown in Fig. 4 were collected using a Mo disk working electrode in a 3-electrode cell containing basic electrolyte at 50% SoC. The V_{app} was cycled between 2.3 V vs Na/Na^+ and the anodic switching potential, which was increased from 3.1 to 3.5 V, at 10 mV s^{-1} (Fig. 4a). Ohmic drop iR_{Ω} was not subtracted here because of the low current densities and to represent plainly the switching potentials. When the switching potential was $V_{\text{app}} = 3.10 \text{ V}$, a single redox couple was observed, as indicated by a single anodic peak (I_{ox}) at $V_{\text{app}} = 2.99 \text{ V}$ and cathodic peak (I_{red}) at $V_{\text{app}} = 2.83 \text{ V}$. This scan window was below the onset potential for the anodic reaction in acidic NaI/AlCl_3 (3.17 V, Fig. 2). The magnitude of i_{pc} was greater than i_{pa} when only the first redox couple was probed. Scanning positive of 3.10 V produced a second anodic peak (II_{ox}) occurring at $V_{\text{app}} = 3.22$ and 3.21 V for switching potentials of 3.30 V (blue) and 3.50 V (red color), respectively. The peak current densities for i_{pa} II_{ox} decreased from 43.8 to 22.7 mA cm^{-2} when the switching potential increased from $V_{\text{app}} = 3.30$ to 3.50 V. While the CV with anodic switching potential 3.30 V (blue) showed two cathodic peaks occurring at 2.87 V (I_{red}) and 3.06 V (II_{red}), the CV to 3.50 V (red) did not have the second cathodic peak (II_{red}). The decreases in i_{p} and the total suppression of II_{red} suggest that the electrode surface became passivated as higher anodic potentials were reached and as more positive current had been passed. However, the peak I_{red} shifted by 40 mV positive when the switching potential increased from $V_{\text{app}} = 3.10$ (black) to 3.30 V (blue). The magnitude of the steady i_{c} below 2.73 V decayed to $<1 \text{ mA cm}^{-2}$ for the 3.10 V switching potential but remained between $3\text{--}4 \text{ mA cm}^{-2}$ for the wider window scans. This observation suggests that anodic potentials above $V_{\text{app}} = 3.10 \text{ V}$ may generate an additional species that is not present in appreciable quantities on or near the electrode surface prior to the higher potential oxidation process in basic electrolytes. This species may form a passivating or blocking layer at the electrode interface.

For the CVs in basic NaI/AlCl_3 (Fig. 4a), several consecutive scans were required before the CV behavior became consistent. This transient CV behavior is shown in Fig. 4b, where the third cycle (red color) was highly suppressed compared to the first cycle (black). Sweeping in the positive direction, the first scan had an initial i transient of -20 mA cm^{-2} at 2.50 V followed by a large anodic branch II_{ox} that reached 270 mA cm^{-2} at the switching potential. On the third scan, the i at the same V_{app} (2.50 and 3.50 V) were -3.6 and 4.3 mA cm^{-2} , respectively. The iR_{Ω} drop was not subtracted here because the electrode potentials and scan rate dependence are not analyzed quantitatively. The transient behavior in basic NaI/AlCl_3 was unlike what was observed in acidic electrolyte, where multiple scans were not required for consistent CV behavior. This suggests that the electrode-electrolyte interfaces were more prone to changes due to iodide redox in basic compared to acidic electrolyte. Basic electrolytes showed two distinct oxidation reactions, with the first occurring as an intermediate to the higher potential process. In the forward direction, the anodic reactions (I_{ox} and II_{ox}) have previously^{9,27} been reported in other electrolytes to be I^- oxidation (Eq. 1) followed by the subsequent oxidation of the intermediate I_3^- ,



However, these species may complex with AlCl_3 and so the reactions should be taken as idealized forms. On the reverse scan, I_2 is reduced to I_3^- and then again to I^- (peaks II_{red} and I_{red} , respectively, Fig. 4a). In acidic electrolyte, it is possible that the two anodic processes overlap in the CVs, or else the second oxidation process occurs at potentials more positive than ones measured here. In basic electrolyte, the high i_{pc} for the reduction of I_3^- (-86 mA cm^{-2}) on the reverse scan precedes the passivated behavior on subsequent scans. The transition to a less active state during CV suggests that the electrode surface in basic NaI/AlCl_3 may be

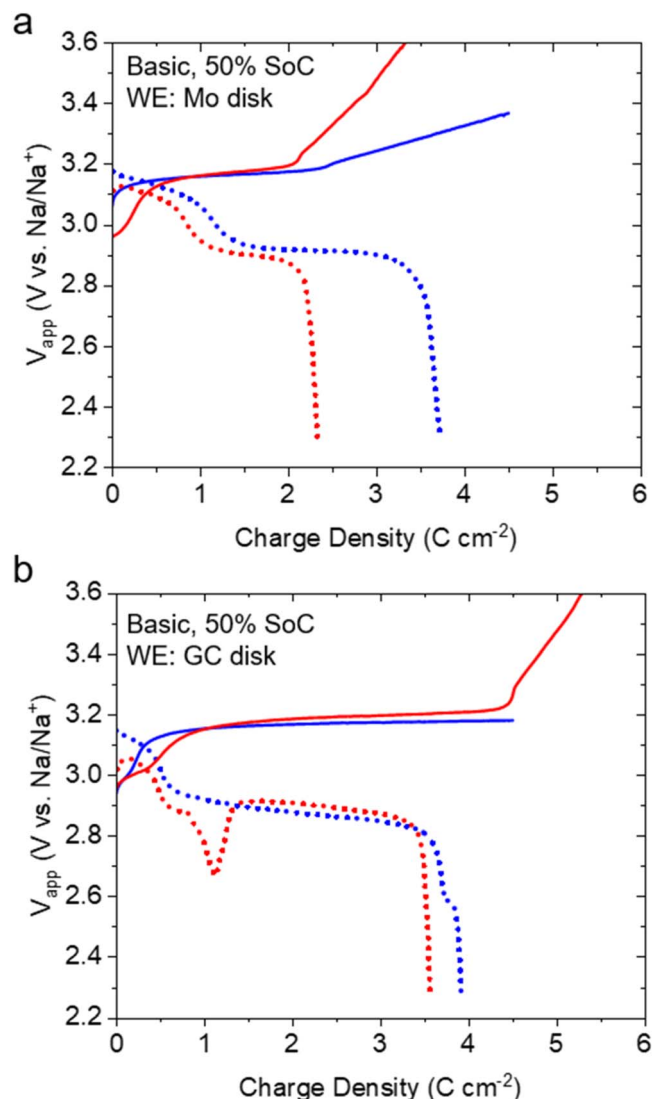


Figure 6. CP at 5 (blue) and 10 (red) mA cm^{-2} for up to 900 s on (a) Mo and (b) GC disk working electrodes. The electrolyte was basic NaI/AlCl_3 at 50% SoC. Positive current (solid lines) preceded negative current (dotted lines) with 60 s open circuit rest between each CP measurement. V_{app} limits were 2.3–3.6 V.

blocked by rapidly generated NaI , which is thermodynamically stable as a solid at 110°C (Fig. S6). Alternatively, it is possible that I_2 or I_3^- generated on the anodic forward scan is not fully reduced on the reverse scan on the first cycle, as indicated by the small reduction charge (2 C cm^{-2}) that followed oxidation (8 C cm^{-2}). That the surface layer partly remained intact during reduction and was not able to be oxidized on the following forward scans, suggests that the film may be I_2 —rather than the more easily oxidized NaI . This interpretation is corroborated by the effect of increasing the switching potential (Fig. 4a), where additional I_2 would be produced at higher potentials. Moreover, the charge transfer kinetics were asymmetric in acidic NaI/AlCl_3 as well, despite the fully molten electrolyte at equilibrium (Fig. S6). Previously, Hubbard et al. detected thin, non-electroactive adsorbed layers of I^- and I_2 on Pt.³⁷ Hanson and Tobais suspected the adsorbed layers as the source for the asymmetry in charge transfer of reaction I_{ox} compared to I_{red} , since additional η_s would be required to overcome the adsorbed I_2 .⁹ More CVs showing the effects of scan rate and electrode material in basic NaI/AlCl_3 are provided in Fig. S7.

Interfacial stability during chronopotentiometry depends on lewis acidity and SoC.—To examine the stability of the redox reactions occurring on the electrode surface, current densities were applied for 900 s increasing from 5 to 10 mA cm^{-2} at 110°C . Oxidation (+) current was followed by reduction (−) current and 60 s rests at open circuit were used between each CP. Three variables were investigated: (i) working electrode material, (ii) Lewis acidity, and (iii) SoC. Figure 5 compares acidic to basic NaI/AlCl_3 , both at 7.5% SoC, using a Mo disk working electrode. In acidic electrolyte, Mo sustained a small but gradual increase in voltage at both +5 and + 10 mA cm^{-2} (Fig. 5a). After passing 4.5 C cm^{-2} , the surface overpotentials $\eta_s = V_{\text{app}} - E_{\text{eq}} - iR_{\Omega}$ were 34 and 87 mV at +5 and + 10 mA cm^{-2} , respectively. On reduction at -5 mA cm^{-2} (data also shown in Fig. 3a), the voltage profile was slightly less stable than on charge: after 4.5 C cm^{-2} , η_s was -102 mV at -5 mA cm^{-2} , about 3x greater than for the same positive i . The Mo electrode was able to pass only 0.5 C cm^{-2} at -10 mA cm^{-2} in acidic electrolyte at 7.5% SoC before reaching the cutoff voltage, 2.3 V.

Compared to acidic electrolyte, CP in basic electrolyte at 7.5% SoC showed (i) additional voltage profile features and (ii) that less charge could be passed before reaching the cutoff compared to acidic electrolyte (Fig. 5b). The two distinct redox processes found by CV experiments manifested as a “step” in the voltage profiles from 2.95 to 3.15 V during CP between 0.1 and 1 C cm^{-2} , depending on i . Compared to Mo, the step during oxidative CP on GC occurred as a much more gradual process in the same electrolyte, also at 7.5% SoC (Fig. S8). In basic electrolyte, E_{eq} measured at open circuit varied between 2.9 and 3.2 V, depending on the history of the electrode and whether positive or negative current was passed. It is important to mention that the SoC of the electrolyte did not appreciably change during these CP experiments; the total charge passed (1 C at 10 mA cm^{-2}) was negligible compared to the cell capacities (10,800 or 14,400 C). Thus, the step during CP was not due to a change in SoC or bulk composition of the basic electrolyte. It is also evident that the stability of the galvanostatic oxidation and reduction processes were both decreased in basic compared to acidic electrolyte. CP reached the 3.6 V cutoff after 4.81 C cm^{-2} at + 10 mA cm^{-2} in basic electrolyte due to a transition to an accelerated, roughly linear overpotential increase with charge time. This accelerated overpotential increase during oxidation was not seen at + 10 mA cm^{-2} in acidic electrolyte, where at least 9 C cm^{-2} could be passed, independent of the electrode material or SoC. On reduction in basic electrolyte, the voltage dropped rapidly and reached the 2.3 V cutoff after 2.5 C cm^{-2} at -5 mA cm^{-2} . The sharp drop on reduction appears as if the reactant species became unavailable due to concentration depletion, or complete and sudden electrode blocking. This drop was seen in acidic electrolyte as well, but its steepness and appearance in time depended on i , electrode material, and SoC. The possibility of concentration depletion and the need to understand better the electrode behavior motivated examining electrolytes at higher SoC, where the bulk concentration of I_3^-/I_2 is expected to be greater.

Figure 6 shows CP performed on Mo and GC electrodes in basic NaI/AlCl_3 at 50% SoC (electrolyte compositions listed in Table I). When compared to the results at 7.5% SoC, positive current at 50% SoC passed less total charge while negative current passed more charge before reaching the cutoff (cf., Fig. 5 and Fig. S8). This means that the oxidation process was less stable at higher SoC whereas the reduction process was more stable. The step from 3.15 V to 2.9 V on reduction occurred more slowly at 50% SoC compared to 7.5% SoC on Mo. Moreover, this downward step occurred more readily on GC compared to Mo despite the slight additional charge that was passed on GC before reaching the cutoff. The primary differences between GC and Mo in basic electrolyte at 50% SoC are: (i) GC’s ability to pass more oxidative charge density (roughly 4.5 vs 2 C cm^{-2}) before the voltage increased above 3.2 V and (ii) quasi-stability during discharge on GC at -10 mA cm^{-2} ,

where the voltage started to decrease, dropping below 2.7 V, then increased again (cf., Fig. 3a).

The quasi-stable behavior, where the overpotential increases then decreases, is unlike concentration depletion at the electrode surface, which occurs continuously and monotonically as the Nernst boundary layer develops in liquid electrolytes. Note that mass transport to the electrode surface through the liquid electrolyte does not depend on electrode material. However, the mass transport parameter can depend inversely on the size of the WE disk when spherical diffusion plays a role.³⁸ The trends observed for the redox processes on different electrode materials here do not correlate with electrode size. Given (i) the strong dependence on electrode material (also see Fig. 3 and ii) the irregular fluctuations in the overpotential, we conclude that rather than mass transport limitations through the liquid electrolyte, the instability during cathodic CP is more likely due to a NaI layer that blocks the electrode surface. The phase instability in basic electrolytes due to rapid I_2/I_3^- reduction is partially alleviated at higher SoC, where the ratio of $AlCl_3:NaI$ is greater (slightly less Lewis basic) and therefore the Lewis basic NaI is less likely to precipitate. The opposite is true for anodic CP, however, where Lewis acidic I_2 is generated and must react with Lewis basic I^- , forming I_3^- , to easily diffuse into the electrolyte and minimize electrode blocking. Examining these limitations is necessary because the long-term stability of the electrode-electrolyte interface is important for efficient battery operation, where large amounts of charge need to be passed continuously during cycling.

Figure 7 summarizes the stability of CP at 5 and 10 mA cm⁻² across the three variables investigated here: (i) Lewis acidity of the NaI/AlCl₃ (acidic and basic), (ii) two states of charge, 7.5 and 50%, (iii) Mo and GC working electrodes. Asterisks in the figure indicate overpotential increases or voltage fluctuations shown previously. Overall, acidic electrolytes were able to pass oxidative (positive) charge without reaching the cutoff voltage at these current densities for the 900 s oxidation period. Acidic electrolytes could also pass more reduction (negative) charge compared to basic, except at -10 mA cm⁻² and 7.5% SoC. As mentioned earlier, higher SoC enabled more negative charge density to be passed prior to reaching the cutoff voltage. This observation was more obvious at -10 mA cm⁻², but it was also found at -5 mA cm⁻² in basic electrolytes.

Differences in interfacial stability between working electrode materials were in some cases subtle, but several trends deserve summary: (i) the voltage fluctuated on GC, (ii) different SoCs “favored” different materials on reduction, (iii) GC outperformed Mo on oxidation (+) charge in all cases. In acidic electrolyte at 7.5% SoC and -5 mA cm⁻², the voltage behavior on GC showed fluctuations that could not be explained by mass transport limitations in the liquid electrolyte. Similar behavior using GC was observed in acidic electrolyte at 50% SoC and -10 mA cm⁻² (Fig. S8a). In general, Mo passed slightly more negative charge density than GC at 7.5% SoC, while the opposite was true at 50% SoC, where GC outperformed Mo on reduction (battery discharge). Again, GC passed more positive charge density and showed no quasi-stable voltage behavior during oxidation (battery charge). These observations suggest that oxidation and reduction may each generate a different species that can block the electrode, and that Mo and GC electrodes may each be more favorable to a different kind of specific interaction, such as preferential adsorption with a certain species in the electrolyte.³⁹

Film formation identified via increasing rest intervals between electrolysis.—To further interrogate the processes limiting the iodide redox reactions in Lewis basic NaI/AlCl₃ electrolytes, two techniques were employed with increasing rest intervals between electrolysis. First, cathodic current was applied between increasing intervals of rest at open circuit to determine (i) the characteristic time for refreshing the electrode (t_{rx}) after current was passed, (ii) transients in the open circuit voltage, and from these, (iii) what process is likely to limit the stability of the reduction reaction at moderate current densities. Later, EIS will be used in combination with CA

and periods of rest to measure changes in the surface resistance due to redox reactions in molten NaI/AlCl₃. These observations support the hypothesis that film formation is responsible for the detrimental effects that prolonged electrolysis has on electrode behavior.

Figure 8 shows cathodic CP at -5 mA cm⁻² interrupted by increasing periods of rest at open circuit: 10, 60, and 600 s. The WE was a Mo disk and the electrolyte was basic NaI/AlCl₃ at 50% SoC. The charge density Q_j passed before each rest period $j = \{1: 4\}$ is also shown. On the first application of -5 mA cm⁻², Q_1 was -1.35 C cm⁻² before the cutoff voltage (2.3 V) was reached. Then, after 10 s rest, Q_2 for the following period was only -0.117 C cm⁻². After the 60 s rest period, Q_3 was -0.577 C cm⁻², less than half the initial amount reduced, Q_1 . But after a 600 s rest at open circuit, Q_4 was -1.44 C cm⁻², roughly equal to the initial charge passed at -5 mA cm⁻². This indicates that the time for the cell to refresh its initial state—after reduction ceased at the cutoff voltage—was 60 s < t_{rx} < 600 s. The change in the OCV was also an indicator of t_{rx} , where the voltage began to increase from 2.93 V at $t = 700$ s, or 215 s into the 600 s rest period after Q_3 . The cell could not recover the initial OCV of 3.06 V vs Na/Na⁺ until $t = 980$ s, or 450 s into the 600 s rest period. Transient potential behavior at open circuit implies a transition of mixed redox processes whose net current is 0 (i.e., mixed potential theory)⁴⁰ and is associated with slow electrode surface exchange of one species for another.⁴¹ In this case, the transition may be from a chiefly reaction I_{red} product (I^-) on the electrode to an intermediate species (I_3^-), identified using CV above (Fig. 4). The amount of negative charge passed far exceeds the charge of a single monolayer (typically <500 μC cm⁻²), as indicated by the large Q_j , ruling out strong adsorption of monolayers as the reduction-terminating process. Moreover, the time scale for t_{rx} exceeds the typical range for relaxation of concentration gradients via diffusion, $\tau = \delta^2/D \cong 10$ –100 s, where the boundary layer thickness δ is assumed 100 μm and D is roughly 10⁻⁵ to 10⁻⁶ cm² s⁻¹. Rather than diffusion through the liquid electrolyte alone, the surface-blocking film and concurrent non-electrochemical reactions likely play a significant role in modulating concentration gradients and kinetics at the electrode surface. Therefore, in agreement with our conclusion above, the process that inhibits stable reduction ≤ -5 mA cm⁻² in NaI/AlCl₃, is a thick film that builds up at the electrode interface. This film eventually disappears over 600 s, once the reaction ceases or slows below the film dissipation rate, and the electrode surface is refreshed.

To identify changes that occurred on the electrode surface due to the oxidation reactions in basic electrolyte, positive potential steps were applied, followed by cycles of rest at open circuit and potentiostatic EIS. Figure 9 shows the applied voltage V_{app} and resulting current density i for the 3.15 and 3.4 V potential steps along with the intermittent EIS measurements. As before for the interruption of reduction current, this experiment probed (i) the characteristic time t_{rx} for refreshing the electrode after anodic current was passed at two different V_{app} , and (ii) transients in the open circuit voltage. The EIS measurements also enabled (iii) quantifying changes in the electrode impedance, including surface resistance R_s . From these, we can discuss what processes might limit the stability of the oxidation reactions.

Potentiostatic EIS was measured for the Mo WE at open circuit (3.067 V vs Na/Na⁺) prior to the potential steps (Fig. 9b, pt 1). For this initial state of the electrode, R_Ω was 0.58 Ω cm² and R_s was 0.15 Ω cm², as determined from the projected intercepts of the Nyquist plot with the real axis Z' . The potential was then stepped to 3.15 V and the current decayed from 36 to 2 mA cm⁻² with small oscillations in the response shown in the inset. Oscillations in the current response during CA have previously been explained by the electrochemical formation of I_2 and its consumption via Eq. 4.^{10,22,24} After 3.15 V was applied for 600 s, the potential was allowed to float at open circuit for 10 s before EIS was measured again (Fig. 9b, pt 2). Here, R_Ω and R_s increased to 0.65 and 0.51 Ω cm², respectively. The increase in R_s , however, was significantly greater as is evident by a

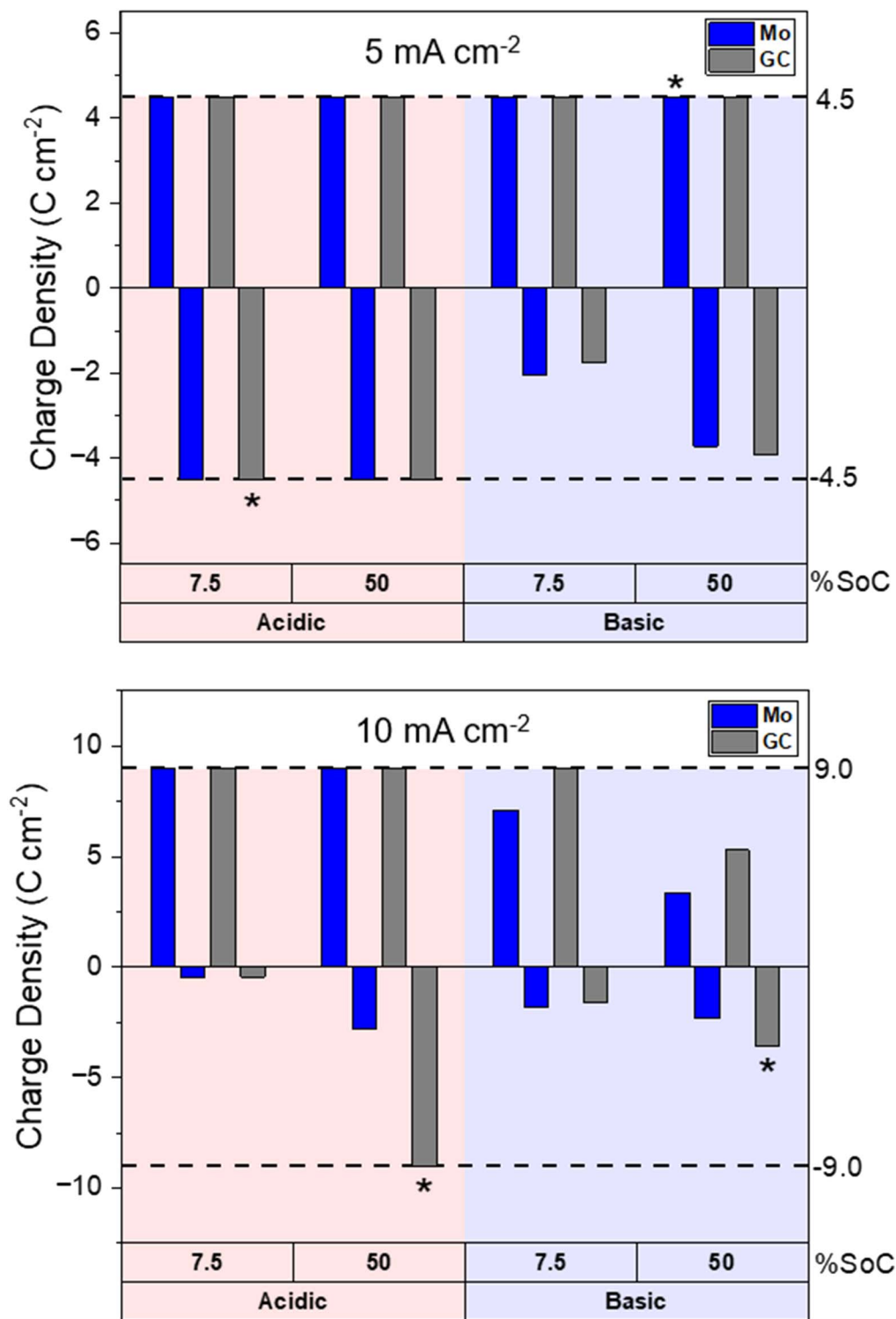


Figure 7. Summary of interfacial stability during CP: amount of charge density passed in 900 s at 5 and 10 mA cm⁻². Acidic NaI/AlCl₃ is on the left (*red background*), while basic NaI/AlCl₃ is shown on the right (*blue background*). Two SoCs, 7.5% and 50%, were tested for each nominal composition. Bars that do not meet the dashed line indicate that V_{app} reached the cutoff before the time limit. Asterisks (*) indicate CP with increasing overpotential on oxidation (positive charge) that would reach the cutoff given more time, or quasi-stable voltage behavior on reduction (negative charge) shown in Figs. 3, 5, 6 and S8.

large increase in the size of the semicircle in the Nyquist plot compared to the small shift to the right. The 240% increase in R_s suggests that the voltage step to 3.15 V and the accompanying +2.1 C cm⁻² significantly changed the electrode surface by adding to it a resistive layer that, based on the small change in R_{Ω} , may have also slightly decreased the active area of the electrode. The change in R_{Ω} could also be explained by a decrease in the ionic conductivity of

the liquid electrolyte; however, this explanation is less plausible given (i) the small amount of charge passed relative to the total volume and capacity of the electrolyte, and (ii) the brief duration of this change. The layer that formed on the electrode here was likely an I_3^- species but could also include I_2 based on the potential, which was between peaks I and II identified earlier in the CVs (see Fig. 4). The open circuit voltage (OCV) slowly drifted back towards the

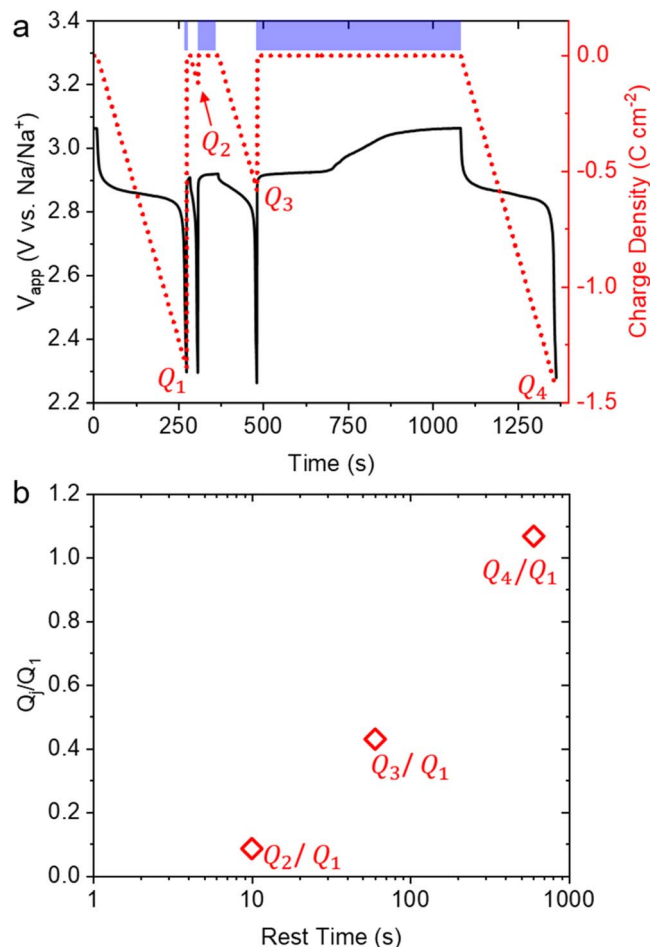


Figure 8. (a) CP at -5 mA cm^{-2} followed by increasing rest times at open circuit: 10, 60, and 600 s (blue bars). The working electrode was a Mo disk and the electrolyte was basic NaI/AlCl₃ at 50% SoC. Voltage (black) and charge density (red, dotted). (b) The ratio of the charge Q_i accumulated during CP after each rest time compared to the initial charge Q_1 .

initial value, reaching 3.073 V by $t = 4800 \text{ s}$ or 2300 s of open circuit. At point 4 (after 1500 s of open circuit), the Nyquist plot overlapped with pt 1, indicating a return to the initial state, i.e., $t \geq t_{\text{rx}}$ despite the slightly higher OCV. This experiment suggests that the characteristic time for refreshing the electrode surface after applying 3.15 V for 600 s was $900 \text{ s} < t_{\text{rx}} < 1500 \text{ s}$.

Next, the applied voltage was stepped to 3.4 V vs Na/Na⁺ and EIS was similarly measured after intervals of rest at open circuit. During the step, i declined from >250 to 100 mA cm^{-2} in 200 s and continued to slowly decline on average over the next 400 s, with sudden increases of up to 50 mA cm^{-2} occurring sporadically. These oscillations were amplified and less regular compared to the ones during the 3.15 V step. In total, $+60 \text{ C cm}^{-2}$ was passed in the 600 s period. After 10 s of open circuit following the 3.4 V hold, EIS was measured again (Fig. 9c, pt 5). Clearly, R_{Ω} and R_s both increased relative to pt 1; their values were both $1.0 \Omega \text{ cm}^{-2}$, indicating 54% and 560% increases in R_{Ω} and R_s , respectively. In addition to these changes, diffusional transport to the electrode surface may have been altered as well, as suggested by the low frequency tail that did not maintain the 45° angle typical of a Warburg element. The value of R_s declined over the periods of rest from pts 6 to 7, but the Nyquist plots did not fully return to overlay with pt 1 even after 2300 s. However, the OCV stabilized at 3.077 V, insignificantly higher than after pt 4. The persistent changes in R_{Ω} and R_s imply that the electrode surface was not refreshed in the time of the experiment, i.e., $t_{\text{rx}} > 2300 \text{ s}$. It is possible that, given more time, the surface would eventually return to its initial state, or else, the surface would

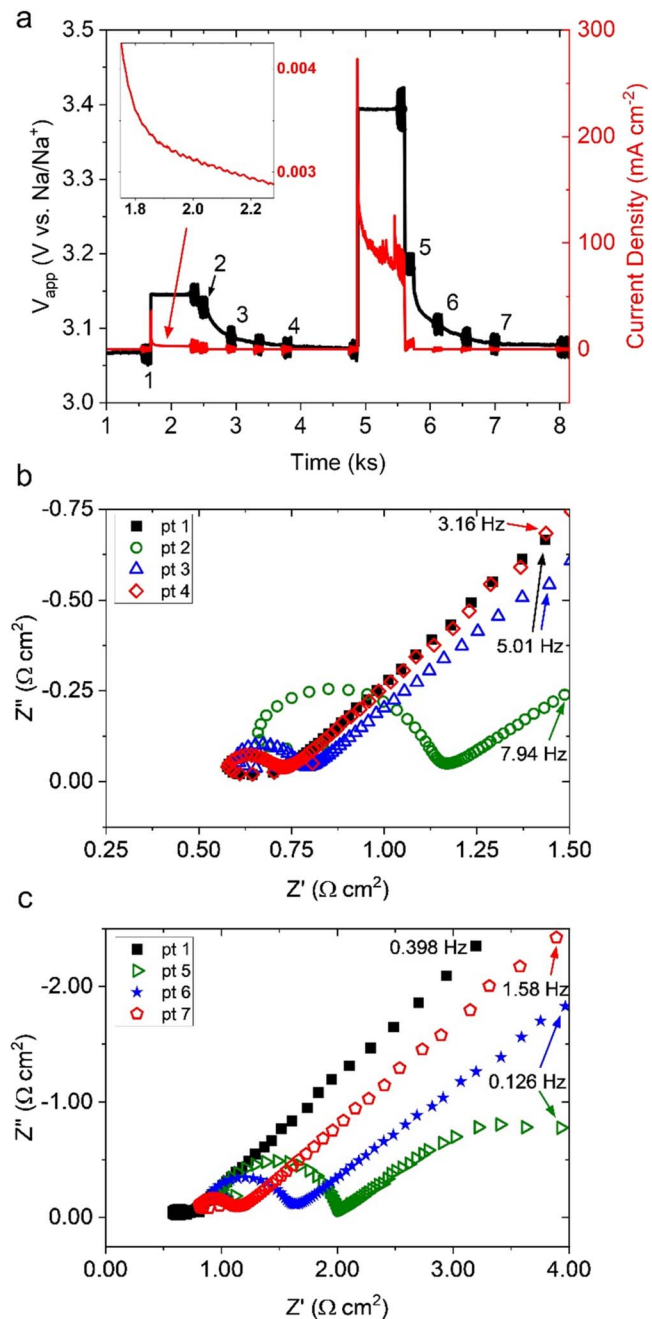


Figure 9. (a) Potential steps from open circuit to 3.15 and 3.4 V vs Na/Na⁺ with potentiostatic EIS taken at various points. Inset shows the current decay during the 3.15 V CA. (b), (c) Nyquist plots taken at the points in time labeled in (a). Labeled EIS measurements were performed at open circuit. The frequency range measured was 1 MHz to 50 mHz; the lowest frequency shown in the plot is labeled and full spectra are shown in the SI. The electrode was a Mo disk and the electrolyte was basic NaI/AlCl₃ at 50% SoC.

need to be refreshed by electroreduction or elevated temperature. The stability of the oxidation process was greatly improved at 120°C (Fig. S10). The details concerning the role of temperature is beyond the scope of this work; however, it is mentioned here to suggest that the buildup of the film on oxidation may be mitigated above the melting point of I_2 (114°C).

In this section it was shown that surface resistance increased during oxidation using potentiostatic EIS following anodic potential steps. Similar experiments were performed for cathodic potential steps, which show that reduction at 2.5 V vs Na/Na⁺ dramatically increased R_s (Fig. S11). This additional surface resistance decreased

after 600 s at open circuit as the mixed potential increased to 2.9 V. These impedance data support the hypothesis that electrode interfacial changes due to film formation during reduction, such as NaI precipitation, greatly influence the redox behavior at time scales relevant to battery cycling.

Conclusions

This work clarifies the roles that (i) electrode material and (ii) molten salt composition play in the electrochemistry of iodide in NaI/AlCl₃ electrolytes at 110 °C. The stabilities of the redox reactions on all electrode materials tested were shown to be strongly influenced and, in some cases, limited by electrode-electrolyte interfacial changes. The electrode surfaces in the NaI/AlCl₃ electrolytes were passivated by electrolytically generated films resulting from both oxidation and reduction. During reduction, the reaction product I[−] formed locally high concentrations of NaI that precipitated a film on the electrode surface. During oxidation, the reaction products (I₂ and possibly higher order polyiodides) built up at the electrode interface, gradually increasing the surface overpotential. Thus, rather than charge transfer kinetics inherent to the electrode material or mass transport limitations through the liquid electrolyte, the greatest barrier to stable and efficient cycling at high rates in these molten salts is the changes that occur at the electrode-electrolyte interface due to the iodide redox reactions.

Of the four candidate electrode materials tested in acidic electrolyte, none showed significant electrocatalytic advantages for iodide redox. Instead, the materials differed chiefly in their ability to resist electrode-electrolyte interfacial changes during redox reactions. Two electrode materials were down-selected based on initial screening in acidic electrolyte: Mo showed the best overall reaction stability on reduction (battery discharge), while GC had the lowest surface overpotential and greatest reaction stability on oxidation (battery charge). In all cases tested, the interfacial instability during reduction was more problematic than that during oxidation. The electrode surface changes and resulting voltage instabilities during CP were generally more pronounced in basic electrolyte, which has less AlCl₃ relative to the iodide/polyiodide species. NaI precipitates formed after less charge had been passed in basic compared to acidic electrolytes at −5 mA cm^{−2}. Moreover, basic electrolytes showed an additional redox process, accessed at higher potentials, that was not seen in acidic electrolytes. This second redox couple produced additional features in the voltage profile during CP, including (i) a voltage step from one redox couple to the other, and (ii) a roughly linear increase in the surface overpotential after passing sufficient positive charge density. Neither one of these issues during oxidation was observed in acidic NaI/AlCl₃ electrolytes on any of the candidate electrode materials tested. Thus, basic electrolytes have worse electrode interfacial stability during oxidation and reduction reactions compared to acidic NaI/AlCl₃.

The electrolyte's state of charge was also shown to have a strong influence on electrode interfacial stability. At lower SoC, the electrolyte is burdened by a higher concentration of I[−] relative to the AlCl₃. Locally high concentrations of I[−] produced at the electrode surface may lead to phase instabilities without sufficient Lewis acid to complex the basic I[−], instead nucleating NaI precipitates. This layer disappeared from the electrode surface over a period of roughly 600 s, as local phase equilibrium was restored, and non-electrochemical processes renewed the interface to its unblocked state. At higher SoC, the electrolyte contains a higher concentration of I₃[−] species and may include some I₂ that has not reacted with I[−], which is in shorter supply. Thus, the electrolyte at high SoC may be more susceptible to locally high concentrations of I₂ that nucleate into electrode-blocking I₂ or other polyiodide films during oxidation. These films also slowly dissipated from the electrode, as evidenced by EIS experiments.

The exact speciation and phase behavior of the NaI/AlCl₃ electrolytes above 0% SoC are currently not well understood. The high absorbance and volatility of these solutions containing high

concentrations of I₂ increases the difficulty of spectroscopic and other optical investigations. However, future studies will attempt to understand more deeply the connection between speciation and electrode-electrolyte interfacial phenomena, including the specific interactions that each electrode material favors with the electrolyte. Also of interest for avoiding surface film formation, from an engineering approach, are (i) high surface area electrodes, which can greatly reduce the charge density accumulated on the electrode during battery cycling, and (ii) elevated temperatures, which may bring the electrolyte to a state of greater phase stability (*i.e.*, above the liquidus line on the phase diagram), mitigating the formation of electrode-blocking films. These parameters will be optimized in future investigations of MNABs using NaI/AlCl₃ electrolytes.

Acknowledgments

The authors thank William Bachman for help with cell fabrication and Philip Mantos for assistance with Sn sputtering. This work was supported by the U.S. Department of Energy's Office of Electricity through the Energy Storage Research Program, managed by Dr. Imre Gyuk. Sandia National Laboratories is a multimission laboratory managed and operated by National Technology and Engineering Solutions of Sandia, LLC, a wholly-owned subsidiary of Honeywell International, Inc., for the U.S. Department of Energy's National Nuclear Security Administration under contract DE-NA0003525. This paper describes objective technical results and analysis. Any subjective views or opinions that might be expressed in the paper do not necessarily represent the views of the U.S. Department of Energy or the United States Government. The employee owns all right, title and interest in and to the article and is solely responsible for its contents. The United States Government retains and the publisher, by accepting the article for publication, acknowledges that the United States Government retains a non-exclusive, paid-up, irrevocable, world-wide license to publish or reproduce the published form of this article or allow others to do so, for United States Government purposes. The DOE will provide public access to these results of federally sponsored research in accordance with the DOE Public Access Plan <https://www.energy.gov/downloads/doe-public-access-plan>.

ORCID

Adam M. Maraschky  <https://orcid.org/0000-0002-9904-098X>
 Stephen J. Percival  <https://orcid.org/0000-0003-2067-7468>
 Rose Y. Lee  <https://orcid.org/0000-0002-2658-7220>
 Melissa L. Meyerson  <https://orcid.org/0000-0001-9327-442X>
 Erik D. Spörke  <https://orcid.org/0000-0003-2286-2560>
 Leo J. Small  <https://orcid.org/0000-0003-0404-6287>

References

1. Y. E. Durmus et al., *Adv. Energy Mater.*, **10**, 2000089 (2020).
2. L. J. Small, A. Eccleston, J. Lamb, A. C. Read, M. Robins, T. Meaders, D. Ingersoll, P. G. Clem, S. Bhavaraju, and E. D. Spörke, *J. Power Sources*, **360**, 569 (2017).
3. M. M. Gross, S. J. Percival, R. Y. Lee, A. S. Peretti, E. D. Spörke, and L. J. Small, *Cell Rep. Phys. Sci.*, **2**, 100489 (2021).
4. J. B. Goodenough, H. Y. P. Hong, and J. A. Kafalas, *Mater. Res. Bull.*, **11**, 203 (1976).
5. Q. L. Ma, C. L. Tsai, X. K. Wei, M. Heggen, F. Tietz, and J. T. S. Irvine, *J. Mater. Chem. A*, **7**, 7766 (2019).
6. N. S. Bell, C. Edney, J. S. Wheeler, D. Ingersoll, and E. D. Spörke, *J. Am. Ceram. Soc.*, **97**, 3744 (2014).
7. M. M. Gross, S. J. Percival, L. J. Small, J. Lamb, A. S. Peretti, and E. D. Spörke, *ACS Appl. Energy Mater.*, **3**, 11456 (2020).
8. M. M. Gross, L. J. Small, A. S. Peretti, S. J. Percival, M. A. Rodriguez, and E. D. Spörke, *J. Mater. Chem. A*, **8**, 17012 (2020).
9. K. J. Hanson and C. W. Tobias, *J. Electrochem. Soc.*, **134**, 2204 (1987).
10. S. Ito, M. Sugimasa, Y. Toshimitsu, A. Orita, M. Kitagawa, and M. Sakai, *Electrochim. Acta*, **319**, 164 (2019).
11. C. Park and J. Chang, *Electrochim. Acta*, **368**, 137650 (2021).
12. G. M. Weng, Z. J. Li, G. T. Cong, Y. C. Zhou, and Y. C. Lu, *Energy Environ. Sci.*, **10**, 735 (2017).
13. B. Li, Z. Nie, M. Vijayakumar, G. Li, J. Liu, V. Sprenkle, and W. Wang, *Nat. Commun.*, **6**, 6303 (2015).

14. F. Bertasi, F. Sepehr, G. Pagot, S. J. Paddison, and V. Di Noto, *Adv. Funct. Mater.*, **26**, 4860 (2016).
15. C. L. Bentley, A. M. Bond, A. F. Hollenkamp, P. J. Mahon, and J. Zhang, *Anal. Chem.*, **88**, 1915 (2016).
16. S. H. Ahn, C. H. Lee, M. S. Kim, S. A. Kim, B. Kang, H. E. Kim, S. U. Lee, and J. H. Banga, *J. Phys. Chem. C*, **121**, 27332 (2017).
17. L. M. Dané, L. J. J. Janssen, and J. G. Hoogland, *Electrochim. Acta*, **13**, 507 (1968).
18. C. H. Lee, E. B. Nam, M. E. Lee, and S. U. Lee, *Nano Energy*, **63**, 103863 (2019).
19. J. D. Newson and A. C. Riddiford, *J. Electrochem. Soc.*, **108**, 699 (1961).
20. C. L. Bentley, A. M. Bond, A. F. Hollenkamp, P. J. Mahon, and J. Zhang, *Electrochim. Acta*, **109**, 554 (2013).
21. C. H. Wang, X. F. Li, X. L. Xi, P. C. Xu, Q. Z. Lai, and H. M. Zhang, *RSC Adv.*, **6**, 40169 (2016).
22. S. Ito, M. Sugimasa, Y. Toshimitsu, A. Orita, M. Kitagawa, and M. Sakai, *J. Electrochem. Soc.*, **169**, 022506 (2022).
23. Y. J. Leem, J. T. Muya, H. Chung, and J. Chang, *J. Electrochem. Soc.*, **167**, 046509 (2020).
24. L. Ma and J. E. Vitt, *J. Electrochem. Soc.*, **146**, 4152 (1999).
25. P. H. Svensson and L. Kloo, *Chem. Rev.*, **103**, 1649 (2003).
26. S. J. Percival, L. J. Small, and E. D. Spörke, *J. Electrochem. Soc.*, **165**, A3531 (2018).
27. C. L. Bentley, A. M. Bond, A. F. Hollenkamp, P. J. Mahon, and J. Zhang, *J. Phys. Chem. C*, **119**, 22392 (2015).
28. R. Y. Lee, S. J. Percival, and L. J. Small, *J. Electrochem. Soc.*, **168**, 126511 (2021).
29. A. M. Maraschky, M. L. Meyerson, S. J. Percival, D. R. Lowry, S. Meserole, J. N. Williard, A. S. Peretti, M. Gross, L. J. Small, and E. D. Spörke, *J. Phys. Chem. C*, **127**, 1293 (2023).
30. Y. C. Lee, J. Kolafa, L. A. Curtiss, M. A. Ratner, and D. F. Shriver, *J. Chem. Phys.*, **114**, 9998 (2001).
31. H. A. Øye, E. Rytter, P. Klæboe, and S. J. Cyvin, *Acta Chem. Scand.*, **25**, 559 (1971).
32. M. Davies and E. Gwynne, *J. Am. Chem. Soc.*, **74**, 2748 (1952).
33. K. J. Hanson, M. J. Matlosz, C. W. Tobias, and J. Newman, *J. Electrochem. Soc.*, **134**, 2210 (1987).
34. D. Shen, K. Steinberg, and R. Akolkar, *J. Electrochem. Soc.*, **165**, E808 (2018).
35. E. I. Rogers, D. S. Silvester, L. Aldous, C. Hardacre, and R. G. Compton, *J. Phys. Chem. C*, **112**, 6551 (2008).
36. B. B. Dave, R. E. White, S. Srinivasan, and A. J. Appleby, *J. Electrochem. Soc.*, **140**, 2139 (1993).
37. A. T. Hubbard, R. A. Osteryoung, and F. C. Anson, *Anal. Chem.*, **38**, 692 (1966).
38. W. E. Morf, *Anal. Chim. Acta*, **330**, 139 (1996).
39. D. J. Barclay, *J. Electroanal. Chem.*, **28**, 443 (1970).
40. C. Wagner and W. E. Traud, *Z. Elektrochem. Angew. Phys. Chemie*, **44**, 391 (1938).
41. L. Yu, Z. Vashaei, F. Ernst, and R. Akolkar, *J. Electrochem. Soc.*, **163**, D374 (2016).